water

MDPI

Article

Multi-Scale Dynamics of Permanent Surface Water in the Lower Yangtze River Basin: Basin-Scale Expansion and Pixel-Scale Fragmentation

Jie Yu [1,2], Yiyuan Tian [1,2], Yi Lin [1,2,*], Chen Gao [1,2] and Huan Xie [1]

[1] College of Surveying and Geo-Informatics, Tongji University, Shanghai 200092, China; 2011_jieyu@tongji.edu.cn (J.Y.); tianyiyuan@tongji.edu.cn (Y.T.); gcjnws@163.com (C.G.); huanxie@tongji.edu.cn (H.X.)
[2] Research Center for Remote Sensing Technology and Application, Tongji University, Shanghai 200092, China
* Correspondence: linyi@tongji.edu.cn

Abstract

Permanent surface water is an important component of regional hydrological systems, yet basin-scale area statistics alone may overlook structural changes in highly modified basins. This study investigated long-term permanent surface-water dynamics in the Lower Yangtze River Basin (LYRB), China, during 2000–2020 using a basin-to-pixel remote sensing framework that combined annual water mapping with multi-scale structural diagnostics. Annual permanent surface-water maps were derived from Landsat imagery using adaptive thresholding. The reliability was evaluated through product-level comparison, reference-based accuracy assessment, and representative complex-scene comparisons with machine learning and deep learning baselines in urban-shadow, turbid-water, and algae-affected environments. Basin-scale landscape metrics, centroid migration, and pixel-level Spatial Water Variation (SPAT) indices were constructed to characterize structural change, while generalized additive models were applied to examine changing associations with hydro-climatic, land-surface, and anthropogenic factors. The extracted dataset achieved high overall accuracy (OA = 98.43%) and improved delineation of narrow channels and fragmented littoral boundaries. Permanent surface water in the LYRB followed a decline–recovery–stabilization trajectory, but basin-scale expansion often co-occurred with increased pixel-scale fragmentation and reduced aggregation. Expansion was mainly expressed through scattered small patches, whereas shrinkage was concentrated along the margins of existing water bodies. Driver analysis further showed that NDVI remained the strongest explanatory variable throughout the study period, while land-surface and anthropogenic variables became more prominent in later periods relative to hydro-climatic variables. These results indicate that basin-scale area statistics alone are insufficient to describe the full evolution of permanent surface water and provide a useful multi-scale perspective for understanding permanent surface-water change in highly modified river–lake basins.

Keywords: permanent surface water; scale-dependent change; Lower Yangtze River Basin; remote sensing; fragmentation

Check for updates

Academic Editors: Teodosio Lacava, Elhadi Adam, Wei Jiang, Qingke Wen and Yizhu Lu

Received: 4 June 2026
Revised: 16 July 2026
Accepted: 24 July 2026
Published: 30 July 2026

Copyright: © 2026 by the authors. Licensee MDPI, Basel, Switzerland. This article is an open access article distributed under the terms and conditions of the Creative Commons Attribution (CC BY) license.

1. Introduction

Permanent surface water is a critical component of regional hydrological systems because it provides relatively stable water storage, supports ecosystem functioning, and reflects long-term changes in aquatic environments [1]. In highly modified river–lake

systems, however, changes in permanent water are not expressed only as area gain or loss. They may also involve changes in shoreline configuration, patch connectivity, and localized fragmentation, which are relevant to hydrological stability and landscape integrity. Therefore, analysis of permanent surface water requires attention not only to basin-scale area change, but also to structural change within the water system.

The Lower Yangtze River Basin (LYRB) is one of the most modified river–lake systems in China and represents a critical region for water-resource analysis. As a densely populated economic core, the region faces a pronounced spatial mismatch between water availability and urbanization pressure. In 2024, per capita water resources in the lower reaches were only 704.99 m^3, which was 59.7% lower than the national average [2]. At the same time, extensive land reclamation, infrastructure expansion, and localized ecological engineering have substantially reshaped the natural hydroscape of the LYRB, altering the connectivity and spatial organization of permanent water bodies [3]. These conditions make the LYRB a particularly important basin for investigating the long-term evolution of permanent surface water in a highly modified river–lake system.

Satellite remote sensing, especially when combined with cloud-computing platforms like Google Earth Engine (GEE), has become a widely used approach for regional hydrological monitoring. Extensive research has been conducted on surface-water extraction, employing methods ranging from spectral indices [4] to machine learning and deep learning algorithms [5,6]. While learning-based methods can improve recognition of complex features, they often require large training datasets, substantial computational resources, and careful model transfer across scenes [7]. For long-term and large-area applications, threshold-based approaches combined with spectral water indices remain widely used because of their transparency, computational efficiency and stable performance across long time series. Since the introduction of NDWI by McFeeters (1996) [8], numerous water indices have been developed, including MNDWI, GNDWI, AWEI, EWI, and WI, to improve water discrimination under different environmental conditions [9,10]. Among them, MNDWI has shown particularly strong performance in complex urban environments and large water bodies [11]. Coupled with Otsu thresholding, it has been successfully applied across diverse geographic regions such as India [1], Qinzhou Bay and Manila Bay [12], demonstrating its practical value for regional surface-water mapping. However, most of these studies focus primarily on water extraction accuracy, whereas fewer studies link long-term extraction results with cross-scale structural diagnostics of permanent surface water.

These rule-based strategies have also supported the development of global products like the JRC Global Surface Water (GSW) dataset [13]. However, global consistency inevitably involves a trade-off with local sensitivity. Recent studies have shown that surface-water dynamics can vary strongly across hydrological settings, and that generalized extraction strategies may perform unevenly under local conditions [14]. In the LYRB, highly turbid waters, seasonal algal blooms, urban shadow contamination, narrow channels, and fragmented littoral zones all increase the uncertainty of water delineation [15]. Under these conditions, omission and boundary errors may accumulate, particularly when the objective is to characterize permanent surface water rather than total water extent. This makes locally adapted extraction strategies necessary for improving the spatial integrity of annual permanent water maps in the LYRB.

Despite these advances, understanding long-term permanent surface-water dynamics in complex river–lake systems remains limited by scale and attribution issues. Recent studies have improved long-term surface-water monitoring using indices such as Water Inundation Frequency (WIF) [16], gap-filling strategies [17], and interannual variation indicators [18], providing valuable information on water-area dynamics at regional or

administrative scales. Many existing studies describe water change mainly at the basin or administrative unit scale, which is useful for identifying regional trends but may overlook substantial pixel-level heterogeneity within the same hydrological system [19]. Although pixel-level extraction accuracy has received increasing attention, subsequent analyses often remain focused on aggregated area statistics, leaving localized structural changes such as shoreline retreat, patch fragmentation, and small-patch growth insufficiently characterized. While the absolute accuracy of pixel-level estimates is inherently limited by spatial resolution, especially in narrow channels, mixed pixels, and fragmented littoral zones, retaining the native resolution of Landsat imagery can help avoid spatial homogenization associated with basin-scale aggregation. Recent studies have shown that inundation and water-area dynamics within large floodplain–lake systems can be highly heterogeneous across space and scale [20]. These findings suggest that basin-wide totals may not fully represent internal structural reorganization. In the LYRB, for instance, stable or expanding total water areas could still coincide with localized shoreline retreat, patch fragmentation, or infilling of small water units. Furthermore, water evolution is often simplified to areal gains and losses, whereas structural changes such as fragmentation, aggregation, and shape complexity may provide additional information that is relevant to environmental monitoring and management.

A second limitation concerns driver interpretation. Permanent surface-water evolution is a non-stationary process, and its associations with hydro-climatic variability, land-surface change, and anthropogenic disturbance may vary over time. However, driver analyses are often based on static or linear frameworks, which may be insufficient for describing stage-dependent and nonlinear relationships. Recent regional hydrological studies have emphasized that surface-water responses can differ substantially across environmental settings and may be governed by changing associations rather than uniform controls [21]. In the LYRB, where land-surface transformation and infrastructure expansion have altered the spatial organization of river–lake networks, a key unresolved question is whether the explanatory roles of climatic and anthropogenic factors have shifted over time in ways that are relevant to permanent water stability.

To address these gaps, this study develops a basin-to-pixel analytical framework to investigate the long-term permanent surface-water dynamics in the LYRB from 2000 to 2020. The specific objectives are to: (1) implement a locally optimized adaptive Otsu thresholding method to generate annual permanent surface-water maps with improved spatial integrity; (2) combine basin-scale landscape pattern analysis with four optimized pixel-level Spatial Water Variation (SPAT) indices to characterize water dynamics across scales, thereby linking basin-wide evolutionary trends with localized transition trajectories, shoreline retreat, patch growth, and fragmentation; and (3) employ Generalized Additive Models (GAMs) to quantify the nonlinear and stage-dependent influences of hydro-climatic, land-surface, and anthropogenic drivers on long-term hydrological evolution. The primary contribution of this study is the integration of locally adapted annual permanent-water mapping, macro-scale landscape diagnostics, micro-scale structural indicators, and time-varying driver analysis into a unified cross-scale framework. This framework reveals scale-dependent reorganization of permanent surface water that may be overlooked by basin-scale area statistics alone and clarifies how the explanatory importance of different drivers changes across evolutionary stages.

The remainder of this paper is organized as follows: Section 2 describes the study area and datasets. Section 3 presents the methodology for permanent surface-water extraction and the basin-to-pixel analysis framework. Section 4 reports the results, including accuracy assessment, multi-scale evolution patterns and driver attribution. Section 5 provides the discussion. Finally, Section 6 concludes this paper.

2. Study Area and Data

The LYRB is located in southeastern China (27°08′ N to 34°58′ N, 114°08′ E to 123°08′ E), spanning approximately 938 km from Hukou County in Jiangxi Province in the west to the Yangtze River estuary in the east, with a total drainage area exceeding 120,000 km^2 (Figure 1). The region includes a dense river–lake network composed of large shallow lakes, main-stem and tributary channels, floodplain waters, and numerous small water bodies distributed across the lower Yangtze plain. The LYRB has a typical subtropical monsoon climate with strong seasonality in precipitation. Approximately 75% of annual rainfall occurs between April and September [22,23]. This pronounced wet-season concentration, together with the complex river–lake morphology of the basin, contributes to marked spatial and temporal variability in surface-water distribution [24].

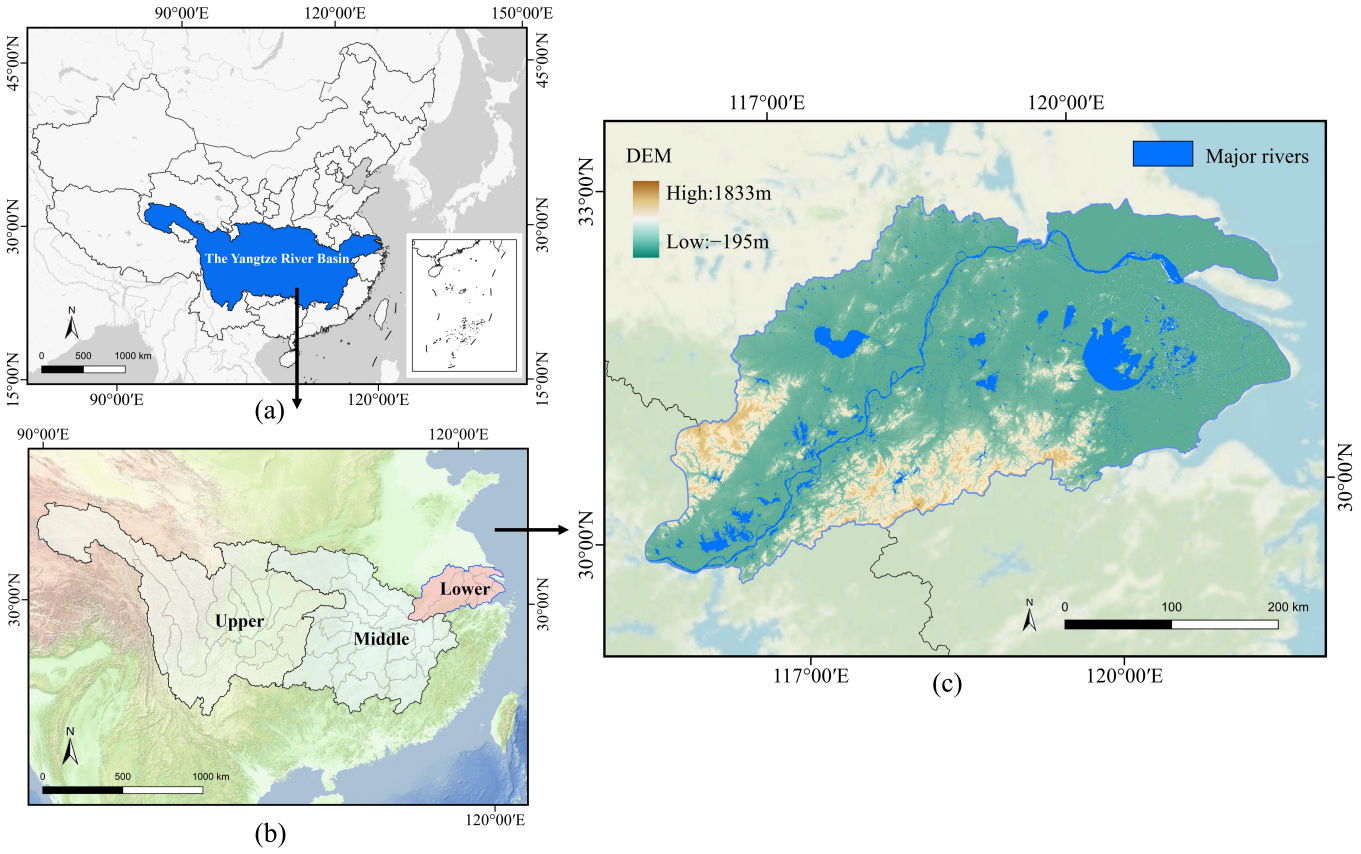


Figure 1. Location and extent of the study area in the LYRB: (**a**) Location of the Yangtze River Basin. (**b**) Upper, middle, and lower reaches of the Yangtze River Basin. (**c**) The LYRB.

To fulfill the research objectives, diverse datasets were integrated, including remote sensing imagery, validation benchmarks, and driving factor variables. Detailed specifications and data sources are provided in Supplementary Table S1. A total of 8400 valid Landsat 5/7/8 images were processed for surface-water extraction (annual image counts are detailed in Supplementary Figure S1). All images were obtained from the Landsat Collection 2 Level 2 standard products, ensuring consistent atmospheric, radiometric, and geometric corrections. For macro-scale comparison and accuracy assessment, the GSW dataset was compared to evaluate long-term trend consistency, while the 10 m ESA WorldCover 2020 dataset was used as a spatial reference for evaluating the classification accuracy.

To evaluate changing driver associations, 13 variables were selected based on two considerations: their widespread application in previous studies of surface-water dynamics and their relevance to the environmental and socioeconomic characteristics of the LYRB. Ac-

cordingly, the variables were categorized into three groups according to their potential roles in influencing permanent surface-water dynamics. Natural factors included hydro-climatic parameters, namely precipitation (Dpre), evaporation (Det), and temperature (Dtem), together with topographic constraints, including elevation (DEM) and slope (SLOPE). The hydro-climatic variables were selected because they directly dictate the regional surface-water balance, while the topographic constraints were included as they control surface runoff routing and local flow accumulation. Anthropogenic factors included socioeconomic and infrastructure indicators, namely population density (POP), gross domestic product (GDP), human activity intensity (HAI), distance to roads (Droad), and distance to railways (Drail). These indicators were chosen to quantify the pressure of human water consumption and the physical alteration in natural drainage networks caused by infrastructure expansion. In addition, NDVI and categorical land-use types were treated as land-surface proxies. Rather than representing direct meteorological drivers, these proxies were used to represent the land-surface conditions associated with vegetation cover, human–environment interactions and land-cover conversions. They were incorporated as potential explanatory variables to quantitatively evaluate their nonlinear associations and relative importance to permanent surface-water dynamics.

3. Methodology

This study combined water mapping with multi-scale hydrological interpretation in four steps (Figure 2): (1) extraction of annual permanent surface water from Landsat imagery using a locally optimized thresholding strategy, (2) evaluation of extracted dataset using both product-level comparison and reference-based accuracy assessment, (3) multi-scale analysis of spatiotemporal dynamics from basin to pixel scale using landscape metrics, centroid migration, and pixel-level Spatial Water Variation indices, and (4) analysis of how the explanatory importance of hydro-climatic, land-surface, and anthropogenic factors changed across four study periods.

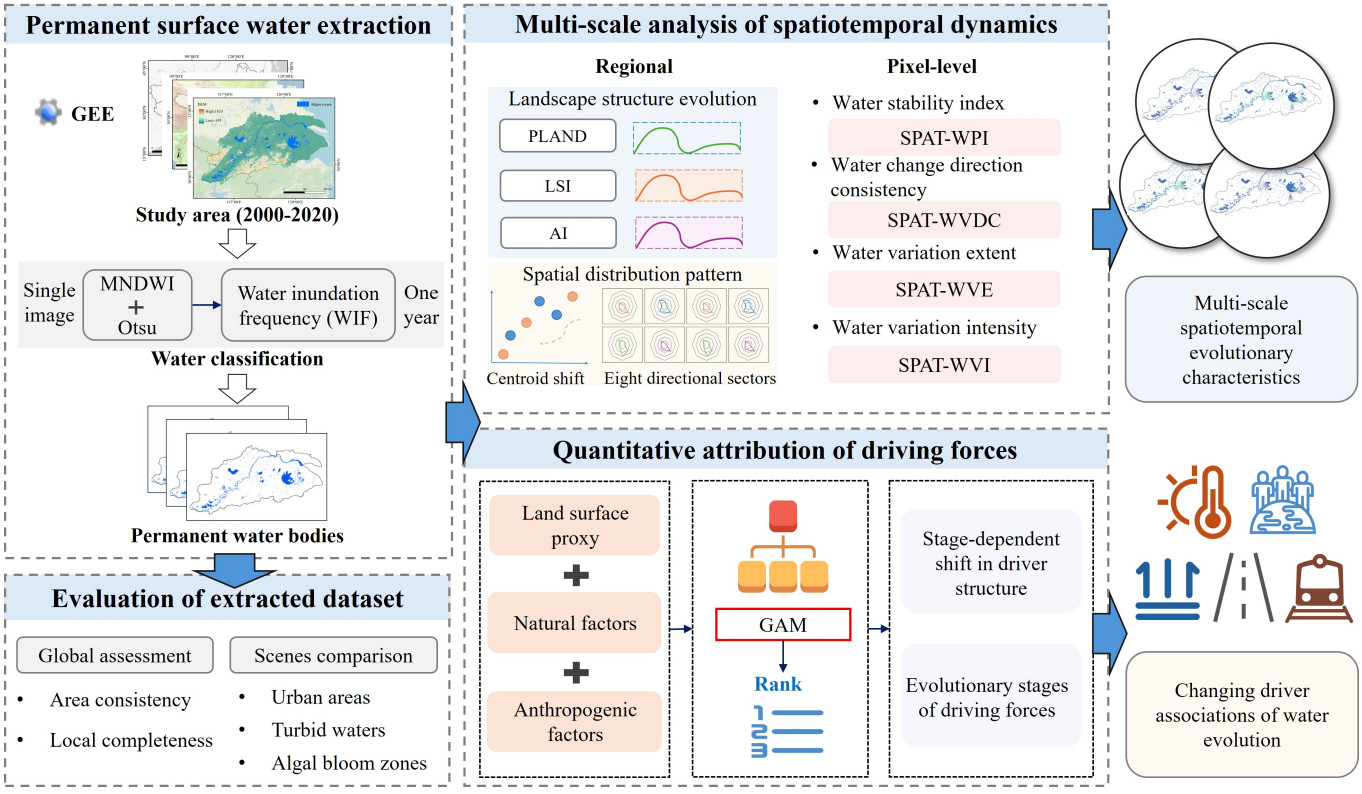


Figure 2. Technical workflow.

3.1. Annual Permanent Surface-Water Extraction

Annual permanent surface water was mapped on the GEE platform using all available Landsat imagery. The procedure included image preprocessing, single-scene water extraction, annual permanent water identification, and accuracy assessment.

1. Image preprocessing: All available Landsat 5, 7, and 8 surface reflectance images were accessed via GEE. Standardized preprocessing was applied to ensure cross-sensor consistency, including conversion of digital numbers to surface reflectance, band alignment, and cloud/shadow masking using the quality assessment band.

2. Water extraction: Single-scene water masks were generated using the MNDWI. MNDWI was selected because it enhances open water by contrasting green and shortwave-infrared reflectance, thereby reducing confusion with vegetation and built-up surfaces. To reduce threshold variation caused by changing surface conditions, an adaptive Otsu method [25] was employed to automatically determine the optimal segmentation threshold by maximizing the inter-class variance between water and non-water pixels for each specific image. Instead of applying a fixed basin-wide threshold, the threshold was locally optimized for individual images, allowing the extraction process to adapt to differences in turbidity, illumination, background land cover, and seasonal surface conditions.

3. Permanent surface-water identification: A Water Inundation Frequency (WIF) metric was calculated to characterize the stability of water presence:

$$\mathrm{WIF} = \frac{\mathrm{WaterNumber}}{\mathrm{TotalNumber}} \quad (1)$$

Pixels with WIF > 0.75 are classified as annual permanent surface water, whereas those with $0.25 < \mathrm{WIF} \leq 0.75$ are classified as seasonal water bodies, serving as the baseline for subsequent analysis [26].

4. Accuracy validation: Validation was conducted in three ways. First, long-term trend consistency was evaluated by comparing annual permanent surface-water area derived in this study with the corresponding GSW trend during 2000–2020. Second, local spatial integrity was assessed in representative heterogeneous zones using high-resolution Google Earth historical imagery, with 2019 regarded as the reference year. Finally, overall quantitative accuracy metrics were calculated using the ESA WorldCover dataset. To reduce inflation of overall accuracy driven by large numbers of pure water or pure land pixels, a stratified random sampling design was implemented, with additional samples allocated to fragmented lake littorals, narrow river channels, and shallow water edges. Overall accuracy was quantitatively evaluated using OA, PA, UA, F1-score, and the Kappa coefficient. To further assess robustness under complex conditions, comparative experiments were conducted across three typical challenging scenes: high-density urban areas, highly turbid waters, and algal bloom zones. The proposed method was compared with four baseline methods: NDWI + Otsu, SVM, RF and DWF. SVM and RF were used as representative traditional machine-learning classifiers, while DWF is a self-training deep learning approach for surface-water percent estimation [27]. The SVM and RF classifiers used the original bands and MNDWI as inputs and were trained using 500 water and 500 non-water points randomly sampled from the GSW permanent water layer. To ensure a reliable and independent evaluation, a total of 1470 water sample points and 1310 non-water sample points were randomly distributed across these scenes and manually labeled based on historical high-resolution Google Earth imagery. In addition, WIF-threshold sensitivity and boundary-buffer analyses were conducted as supplementary uncertainty assessments to evaluate how threshold choice and boundary proximity may influence local permanent-water estimates.

3.2. Framework for Multi-Scale Water Dynamics Analysis

To characterize the spatial heterogeneity of water evolution, a multi-scale analytical framework integrating regional and pixel-level analysis was established, as shown in Table 1.

Table 1. Multi-scale framework for water body pattern analysis across regional and pixel levels.

Scale	Analytical Dimension	Method/Index	Description
Regional	Landscape structure evolution	PLAND [28]	Area-edge index: measures water coverage proportion within the landscape.
		LSI [29]	Shape complexity metric: captures landscape-level edge irregularity and fragmentation.
		AI [30]	Spatial aggregation metric: indicates landscape compactness.
	Spatial distribution pattern	Centroid Shift Model [31]	Analyzes the directional trend and trajectory of water body evolution.
Pixel-level	Local dynamics via moving window	SPAT-WPI	Spatial Water Persistence Index (stability indicator).
		SPAT-WVDC	Spatial Water Variation Directional Consistency Index.
		SPAT-WVE	Spatial Water Variation Extent Index.
		SPAT-WVI	Spatial Water Variation Intensity Index.

3.2.1. Regional Scale Analysis

At the macro scale, spatiotemporal evolution was characterized in terms of landscape structure and directional characteristics. Three landscape metrics (PLAND, LSI, and AI) were calculated in FRAGSTATS 4.2 [32] to quantify water coverage proportion, shape complexity, and spatial aggregation, respectively (Table 1). The centroid model was then employed to compute the annual geometric center of water bodies and track migration trajectories [31]. To further describe the direction and intensity of regional water body changes, the study area was partitioned into eight directional sectors.

3.2.2. Pixel-Level Scale Analysis

To examine local heterogeneity that may be obscured by basin-scale statistics, a pixel-based multi-dimensional evaluation system was constructed using moving-window analysis. A 450 m × 450 m square window was adopted to balance local spatial detail and analytical stability. Within each window, four indices were used to characterize different aspects of permanent surface-water dynamics. First, the Spatial Water Persistence Index (SPAT-WPI) was constructed to quantify the long-term temporal stability:

$$\text{SPAT-WPI} = \sum_{T_1}^{T_2} \text{PW}_t(\text{Pixel}_i) \quad (2)$$

where $\text{PW}_t(\text{Pixel}_i)$ denotes the permanent water status of pixel i in a given year. Based on the 21-year monitoring period, the index ranges from 0 to $T_2 - T_1 + 1$, and the results are classified into four levels: highly unstable (0–5 years, occurrence < 25%), intermittently stable (5–10 years, 25–50%), moderately stable (10–15 years, 50–75%), and highly stable (15–21 years, >75%).

Second, the Spatial Water Variation Direction Consistency Index (SPAT-WVDC) was developed to characterize the local clustering of change direction. The central pixel was defined by differencing surface-water maps between the beginning and end of the study period (expansion = +1, shrinkage = −1, no change = 0). SPAT-WVDC represents the proportion of neighboring pixels sharing the same change direction as the central pixel:

$$\text{SPAT-WVDC} = \frac{\Delta\text{PixelC}_{t_i}}{\text{ChangePixelCount}_{t_i}} \tag{3}$$

$$\Delta\text{PixelC}_{t_i} = \begin{cases} \text{SEPixelCount}_{t_i}, & \text{PixelState}_C = 1 \\ \text{SSPixelCount}_{t_i}, & \text{PixelState}_C = -1 \\ 0, & \text{PixelState}_C = 0 \end{cases} \tag{4}$$

where $\text{SEPixelCount}_{t_i}$ and $\text{SSPixelCount}_{t_i}$ denote the numbers of expanding and shrinking pixels within window I that share the same change direction as the central pixel, respectively; $\text{ChangePixelCount}_{t_i}$ is the total number of changed pixels within the window (excluding the central pixel). PixelState_C represents the change state of the central pixel. The results are divided into five classes: random distribution (0–20%), weak clustering (20–40%), moderate regularity (40–60%), strong directional patterns (60–80%), and dominant consistency (80–100%).

Finally, two indices were used to spatially quantify the magnitude and intensity of surface-water changes at the pixel level: the Spatial Water Variation Extent Index (SPAT-WVE) and the Spatial Water Variation Intensity Index (SPAT-WVI):

$$\text{SPAT-WVE} = \frac{\left|\text{PixelC}_{I_{t_2}} - \text{PixelC}_{I_{t_1}}\right|}{\text{PixelC}_{I_{t_1}}} \times 100\% \tag{5}$$

For a square window with side length Q, SPAT-WVI can be rewritten as follows:

$$\text{SPAT-WVI} = \frac{\left|\text{PixelC}_{I_{t_2}} - \text{PixelC}_{I_{t_1}}\right|}{Q \times Q} \times \text{res}^2 \times 100\% \tag{6}$$

where $\text{PixelC}_{I_{t_2}}$ and $\text{PixelC}_{I_{t_1}}$ denote the numbers of water pixels within window I at periods t2 and t1, respectively. Positive and negative values of $\text{PixelC}_{I_{t_2}} - \text{PixelC}_{I_{t_1}}$ correspond to expansion and shrinkage intensity, respectively, and res^2 represents the area of a single pixel. SPAT-WVE reflects the relative magnitude of surface-water change rather than its direction. SPAT-WVI represents the intensity of net water change normalized by the area of the spatial unit. The two indices were used together to distinguish proportional water variation and absolute disturbance intensity at the pixel level.

3.3. Driving Factors' Quantification for Hydrological Evolution

To evaluate how the explanatory importance of natural, land-surface, and anthropogenic factors changed in relation to permanent surface-water dynamics, Generalized Additive Models (GAMs) were employed. GAMs were used because they can represent potentially nonlinear relationships between water dynamics and environmental variables [33]. Compared with linear regression, GAMs allow each explanatory variable to be fitted using a smooth function without imposing a predefined linear relationship, which is suitable for complex hydro-environmental systems where driver responses may be nonlinear. Thirteen potential driving factors were incorporated and categorized into three functional groups: natural factors, anthropogenic factors, and land surface proxies (as detailed in Section 2). All factors were resampled to a standardized 500 m × 500 m grid to ensure consistency in spatial resolution.

A forward stepwise selection approach was adopted to construct the optimal model. First, single-factor models were tested to identify the primary driving factors with the highest deviance explained. Second, remaining driving factors were iteratively added to the model. A factor was retained only if it significantly improved model performance ($p < 0.05$) and reduced the Akaike Information Criterion (AIC). Independent models were

constructed for four distinct periods (2000–2005, 2005–2010, 2010–2015, 2015–2020), generally formulated as follows:

$$S_{\text{period}} = f_1(\text{Factor}_1) + f_2(\text{Factor}_2) + \cdots + f_N(\text{Factor}_N) + \tau \quad (7)$$

where $\mathbf{f}(\cdot)$ denotes the smooth function (thin plate regression splines), and τ is the error term.

Model performance and factor importance were summarized using factor contribution ranking (Rank), Accumulated Deviance Explained (ADE), AIC, and Adjusted R-squared (Adj. R^2). Rank reflects the relative importance of each driving factor. ADE measures the cumulative contribution of predictors. AIC evaluates the balance between model fit and complexity. Adj. R^2 assesses explanatory power while correcting for degrees of freedom, preventing artificial inflation of model performance and reducing the risk of overfitting.

4. Results

4.1. Accuracy Assessment and Interannual Dynamics

4.1.1. Result Validation and Reliability

The extracted permanent surface-water dataset showed high overall reliability (Table 2). Compared with the GSW product, the proposed method achieved slightly higher overall accuracy (OA) of 98.43%, a Kappa coefficient of 0.8852, and user's accuracy (UA), indicating fewer commission errors. The extracted water area also showed a strong linear correlation with the GSW dataset (Figure 3a), confirming reliable interannual stability. At the local level, the proposed results preserved continuous water extents and narrow-channel continuity more effectively in representative regions such as Changdang Lake, Longgan Lake, and Huazikou River (Figure 3b), although small water features and complex shorelines remained important sources of difference between products.

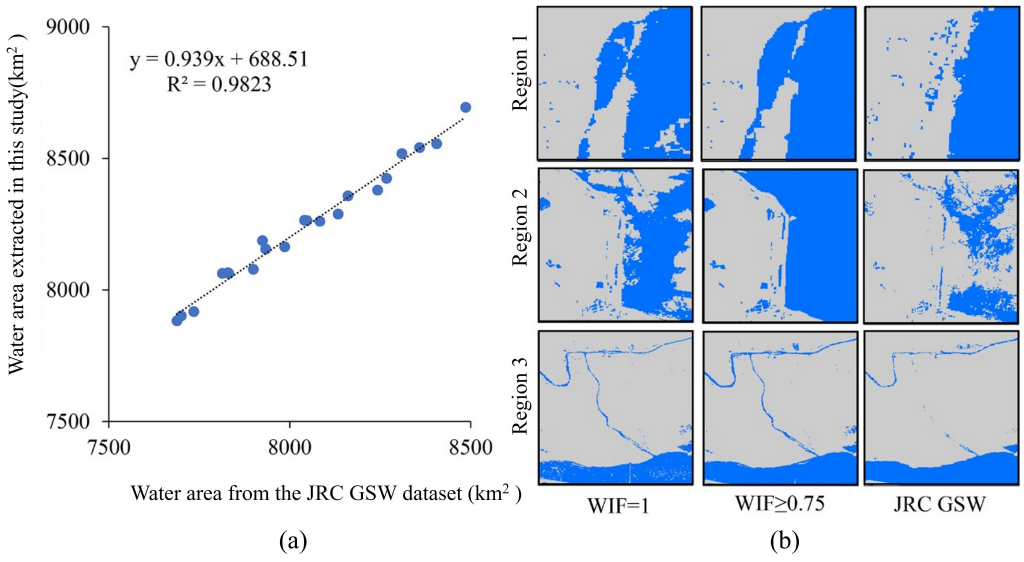


Figure 3. Assessment for the extracted permanent water bodies: (**a**) Quantitative assessment of area consistency. (**b**) Local integrity validation (WIF: water inundation frequency).

Table 2. Accuracy comparison between the extracted results in this study and the GSW dataset.

Water Body Maps	OA (%)	PA (%)	UA (%)	Kappa
Extraction results from this study	**98.43**	**81.91**	**98.31**	**0.8852**
GSW dataset	98.24	81.47	96.16	0.8727

Note: Bold numbers represent the highest accuracy in each column.

To further evaluate performance under representative complex conditions, validation samples from the selected complex scenes were pooled to compare the overall accuracy of different extraction methods (Table 3). The proposed method achieved the highest OA (90.46%), F1-score (90.25%), and Kappa coefficient (0.8093), indicating the best overall balance between omission and commission errors. DWF produced the highest UA (99.20%) but a lower PA (82.20%), suggesting a more conservative extraction tendency. NDWI + Otsu, SVM, and RF showed slightly lower OA, F1-score, and Kappa values than the proposed method. These results indicate that the proposed method maintained a more balanced overall performance across representative complex scenes.

Table 3. Overall accuracy comparison of different water extraction methods across representative complex scenes.

Method	OA (%)	PA (%)	UA (%)	F1 (%)	Kappa
Proposed method	**90.46**	**87.58**	93.08	**90.25**	**0.8093**
NDWI + Otsu	88.85	84.06	93.16	88.38	0.7772
RF	87.91	81.34	93.87	87.16	0.7585
SVM	87.71	80.94	93.84	86.92	0.7545
DWF	90.08	82.20	99.20	89.91	0.8032

Note: Bold values represent the optimal results achieved by the proposed method in terms of OA, PA, F1, and Kappa.

The visual comparison in Figure 4 further illustrates the local behavior of different methods under typical sources of spectral confusion. Across the three complex scenes, the proposed method performed more consistently than the comparison methods, particularly in suppressing shadow-related commission errors and preserving narrow-channel continuity. Specifically, in urban areas (S1–S2), it effectively suppressed shadow interference and maintained the continuous spatial connectivity of micro-water networks. In turbid waters (S3–S4), it better delineated permanent main channels and dynamic shoals than RF and SVM. In algal bloom zones (S5–S6) where floating algae cause severe vegetation-like spectral confusion across all baselines, the proposed method also provided more plausible water boundaries than the baseline methods. Together, the pooled accuracy comparison and visual examples show that the proposed method achieved competitive quantitative performance while retaining better local spatial integrity in complex river–lake scenes.

Supplementary uncertainty analyses further showed that classification uncertainty was mainly associated with transitional and boundary-rich environments. The WIF-threshold sensitivity analysis indicated that changing the WIF threshold from 0.70 to 0.80 produced relatively small mean area differences in five of the six representative scenes (0.45–3.36%). However, S4, representing a turbid-water lake–river transition zone, showed much higher sensitivity, with a mean difference of 20.14% and a maximum difference of 41.38% (Table S6). This indicates that WIF-threshold uncertainty is mainly amplified in shallow, transitional, and boundary-complex water environments. The boundary-buffer analysis further showed that 72.4–79.0% of changed pixels were located within the 30 m buffer of water-body boundaries, and 82.4–87.6% were located within the 60 m buffer (Table S7). These results suggest that uncertainty mainly affected local boundary delineation and transitional water pixels, rather than representing a spatially uniform error across the basin.

4.1.2. Long-Term Extraction Results and Interannual Dynamics

Figure 5 illustrates the extraction results of permanent surface-water in the LYRB from 2000 to 2020. The area averaged 8239 km^2 over the 21-year period, ranging from a minimum of 7883 km^2 in 2001 to a maximum of 8694 km^2 in 2016. The temporal trajectory reveals three distinct phases: (1) From 2000 to 2014, the long-term tendency was downward despite year-to-year fluctuations. Significant contractions occurred in 2000–2001 (−3.54%),

2003–2004 (−4.10%), and 2010–2011 (−3.78%), reflecting a period of net contraction in permanent surface water. (2) From 2014 to 2016, a sharp reversal occurred, with the total area expanding from 7901 to 8694 km^2. This recovery was primarily driven by a substantial surge in 2014–2015 (+8.28%), making the largest single-year increase observed. (3) After 2016, the water area remained relatively stable, fluctuating narrowly between 8261 and 8694 km^2. Overall, the LYRB showed a decline–recovery–stabilization pattern in permanent surface water over the study period. This temporal trajectory provides the basin-scale context for the subsequent analysis of spatial reorganization.

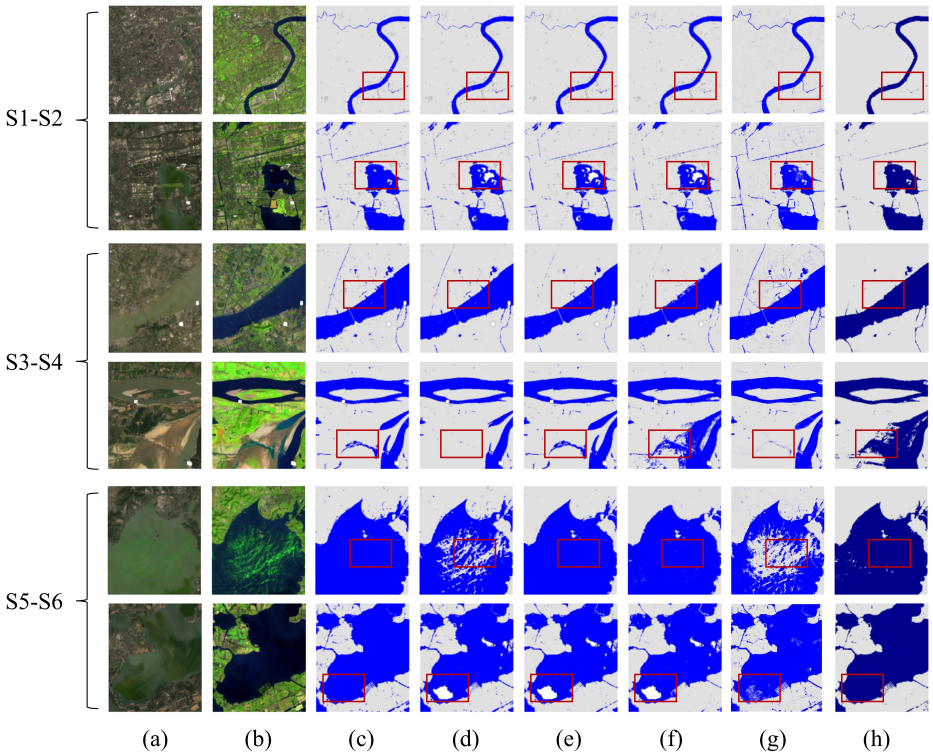


Figure 4. Visual comparison of different water extraction methods in typical complex scenes. (**a**) Original true-color image. (**b**) False-color composite image (SWIR1, NIR, Red). Extracted water bodies using: (**c**) the proposed method, (**d**) NDWI + Otsu, (**e**) SVM, (**f**) RF, (**g**) DWF, and (**h**) GSW.

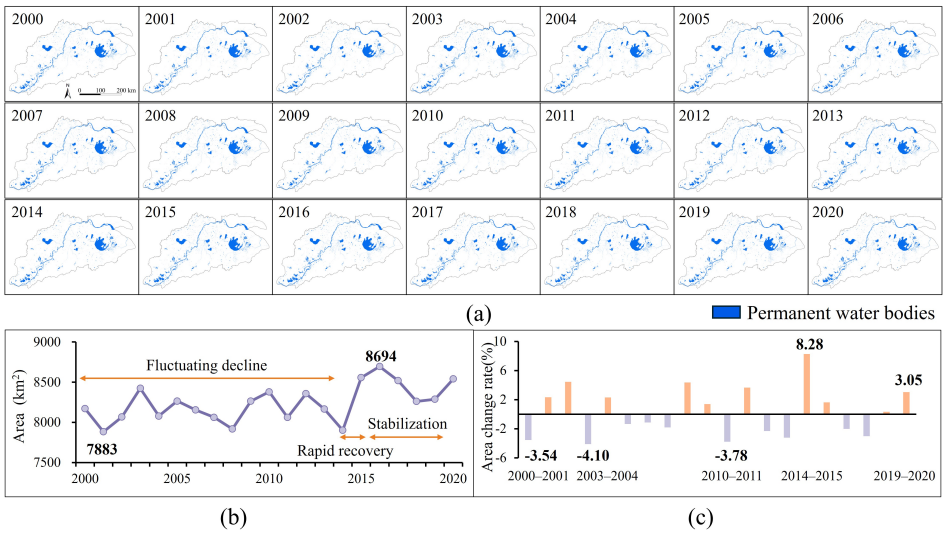


Figure 5. Spatiotemporal dynamics of permanent water bodies in the LYRB (2000–2020). (**a**) Extraction results of permanent water bodies in the LYRB. (**b**) Area of permanent water bodies. (**c**) Change rate of permanent water area.

4.2. Multi-Scale Spatiotemporal Evolutionary Characteristics

4.2.1. Regional-Scale Dynamics Analysis

The three landscape metrics indicate that basin-scale change was accompanied by structural reorganization (Figure 6). PLAND was positively correlated with LSI (r = 0.70), whereas AI showed negative correlations with both PLAND (r = −0.62) and LSI (r = −0.99). This pattern suggests that areal expansion was often associated with increased shape complexity and reduced aggregation, rather than uniform infilling of existing water bodies. In 2003, 2008, and 2014, synchronous local minima of LSI and PLAND coincided with local peaks in AI, indicating that water contraction during those years was associated with a more concentrated configuration of the remaining permanent water bodies. Thus, the long-term trend was predominantly driven by the changes in small-scale water patches rather than the uniform expansion of large water bodies.

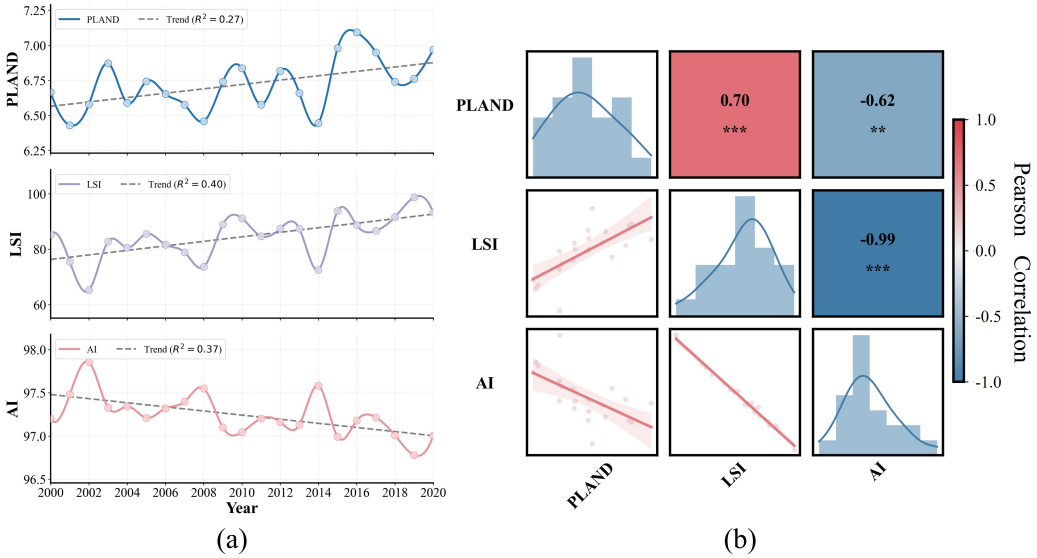


Figure 6. Trends and correlations of landscape metrics (2000–2020). (**a**) Landscape metrics trend. (**b**) Correlation matrix of three landscape metrics. Asterisks indicate statistical significance levels: ** $p < 0.01$, *** $p < 0.001$.

Stage-specific statistics further show that expansion dominated from 2000 to 2015, peaking between 2010 and 2015 with a net increase of 176.2 km^2 (expansion exceeding shrinkage by 36.72%) (Figure 7). However, an opposite trend emerged from 2015 to 2020. Compared with the preceding interval, the shrinkage area increased sharply by 35.95%, resulting in a net loss of 14.5 km^2. Directional analysis shows that for the expansion process, the Directional Disturbance Intensity (DDI) consistently peaked in the southwest (SW) direction, identifying it as the primary zone of spatial restructuring. Conversely, the south (S) and southeast (SE) sectors exhibited high Directional Relative Change Ratio (DRCR) values despite lower DDI, representing a substantial intensification relative to their limited initial water storage. For shrinkage, the period of 2015 to 2020 witnessed simultaneous surges in both DDI and DRCR in the north (N) and northwest (NW) directions, reflecting a concentrated and directionally coherent retreat rather than a gradual background decline. The cumulative asymmetry between expansion and shrinkage vectors ultimately drove a consistent northeast-to-southwest (NE-to-SW) migration of the permanent surface-water centroid throughout the study period. Taken together, these results show that basin-scale area change was accompanied by simultaneous reorganization of spatial structure.

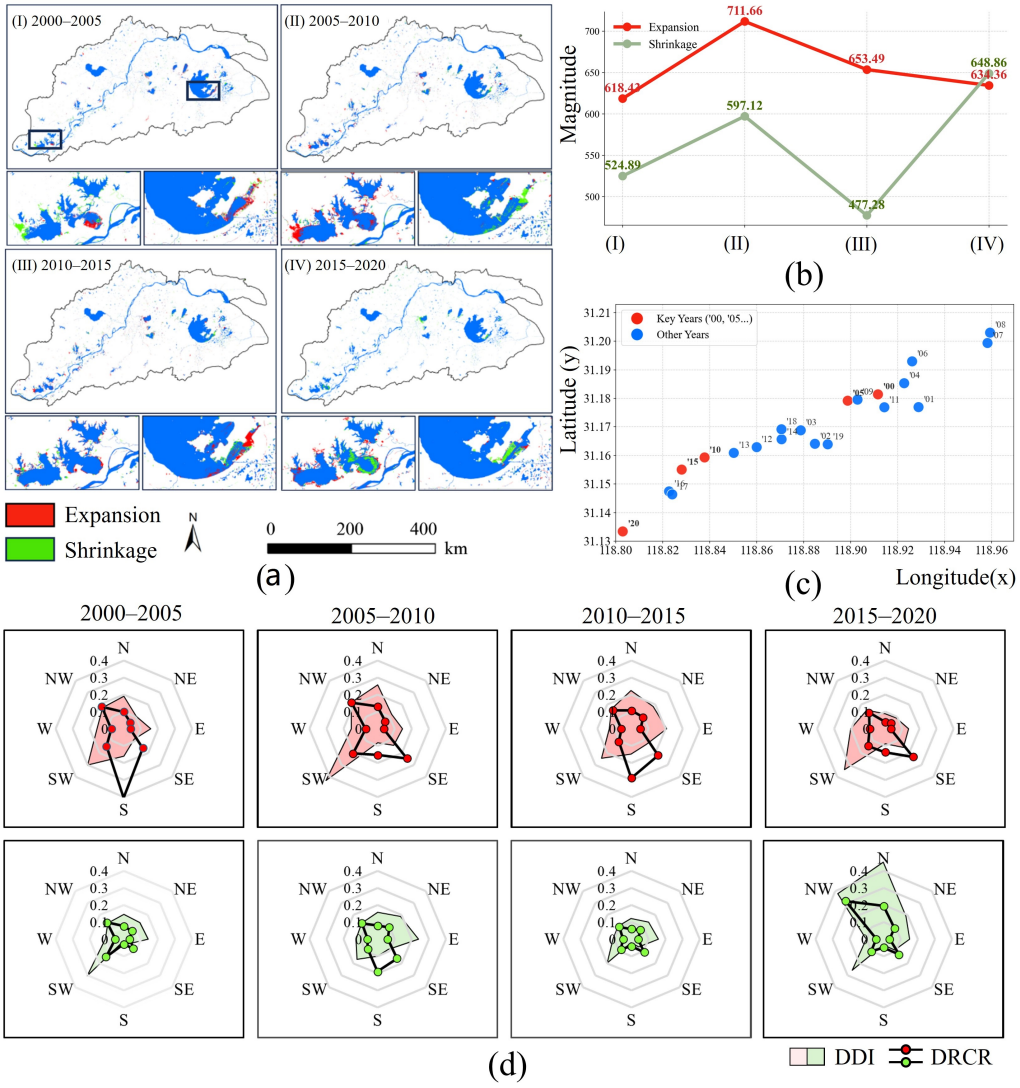


Figure 7. Spatial and areal changes in permanent water bodies in the LYRB from 2000 to 2020: (**a**) Temporal trends of landscape-scale expansion and shrinkage areas across different periods. (Blue areas represent common water bodies present in both years). (**b**) Areas of surface-water expansion and shrinkage in each period. (**c**) Migration trajectory of the centroid of surface-water distribution during 2000–2020. (**d**) Directional evolution characteristics of permanent surface-water expansion (red) and shrinkage (green).

4.2.2. Pixel-Level Scale Dynamics Analysis

Pixel-level scale analysis further clarified the internal structure of permanent surface-water change. Based on the SPAT-WPI index, highly stable water pixels accounted for 75.58% of the total area and were concentrated along the Yangtze River main stem and large lakes such as Taihu Lake and Chaohu Lake (Figure 8). Surrounding these stable cores are transitional belts of moderately (Level III, 7.40%) and intermittently (Level II, 7.13%) stable pixels. In the more intensively urbanized eastern part of the basin, Region 3 exhibited a much more fragmented stability pattern than the contiguous structures in Regions 1 and 2.

The pixel-level directional consistency (SPAT-WVDC, Figure 9) demonstrates that in most periods, over 80% of changing pixels fell within the high-consistency class (>75%). However, a clear exception occurred during 2005-2010, when the proportion of expansion pixels within the high-consistency class dropped sharply to 32.17%, while that in moderate-consistency classes exceeded 61%. This abrupt statistical shift indicates that local

expansion during that period became more fragmented and spatially dispersed than in the other periods.

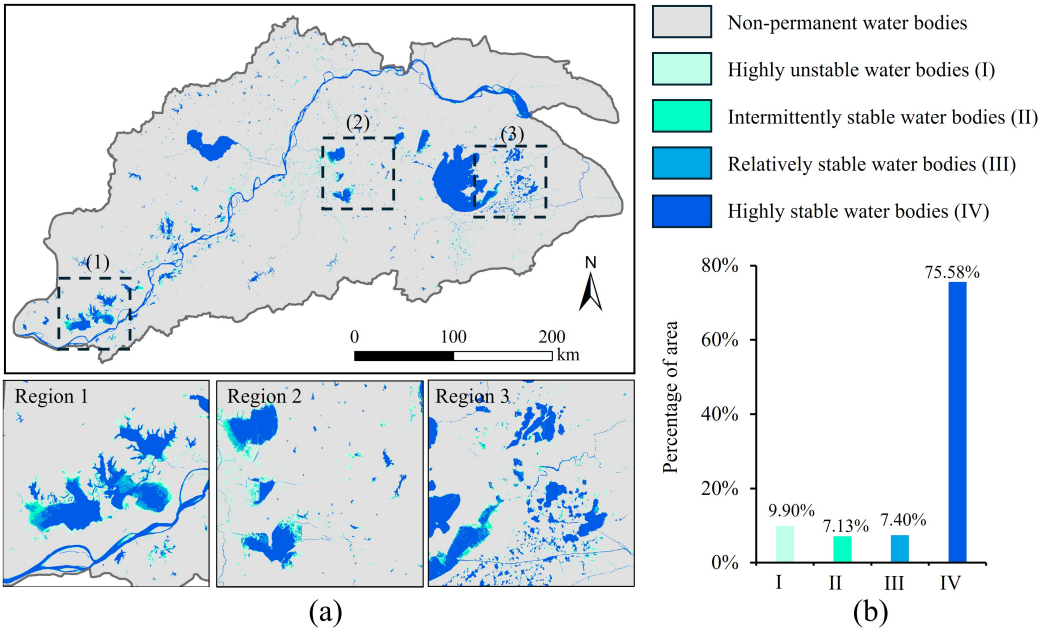


Figure 8. Stability patterns and classification of permanent water bodies in the LYRB (2000–2020): (**a**) Results of SPAT-WPI index. (**b**) Stability levels.

The SPAT-WVE and SPAT-WVI further reveal that expansion (Figure 10) and shrinkage (Figure 11) followed different local pathways. Most pixels experienced low-to-moderate relative expansion (blue), but approximately 15% exhibited very high proportional changes (90% to 100%), primarily in marginal zones and scattered small patches. Notably, from 2000 to 2005, the high proportion of 100% WVE values suggests that expansion predominantly occurred through the emergence of new water pixels rather than incremental growth from pre-existing water bodies. The frequency distribution of SPAT-WVE (Figure 10c) further confirms that pixels with small relative expansion dominate the landscape (in all periods, >60% of pixels have SPAT-WVE < 40%), whereas pixels with high relative expansion are spatially limited. In contrast, high-intensity expansion (SPAT-WVI) manifested as scattered hotspots rather than broad zones (Figure 10b). Local-scale analysis highlights a distinct spatiotemporal shift of these hotspots: from concentrated, belt-like expansion along the Longgan–Huangda–Bo Lake shorelines (Region 1) in the early period (2000–2005) to a dispersed, multi-focal pattern in Taihu Lake (Region 2) during later stages.

Shrinkage, by contrast, was concentrated along the margins of pre-existing water bodies, particularly within littoral zones and shallow-water areas (Figure 11). Low-magnitude shrinkage (SPAT-WVE < 20%) accounted for more than 50% of pixels in most periods, while low-intensity shrinkage (SPAT-WVI < 20%) generally exceeds 80%. This demonstrates that water loss in the LYRB was characterized by gradual shoreline retreat rather than the complete disappearance of whole water bodies. The spatial pattern of SPAT-WVI (Figure 11b) further demonstrates that shrinkage hotspots (SPAT-WVI > 50%) are spatially fragmented and discontinuous, implying that intense shrinkage events are stage-specific and spatially sporadic rather than a basin-wide pervasive phenomenon. Over time, the spatial configuration of high-intensity shrinkage evolved from relatively clustered patch-like patterns in the early stage to more dispersed point-like patterns in later stages.

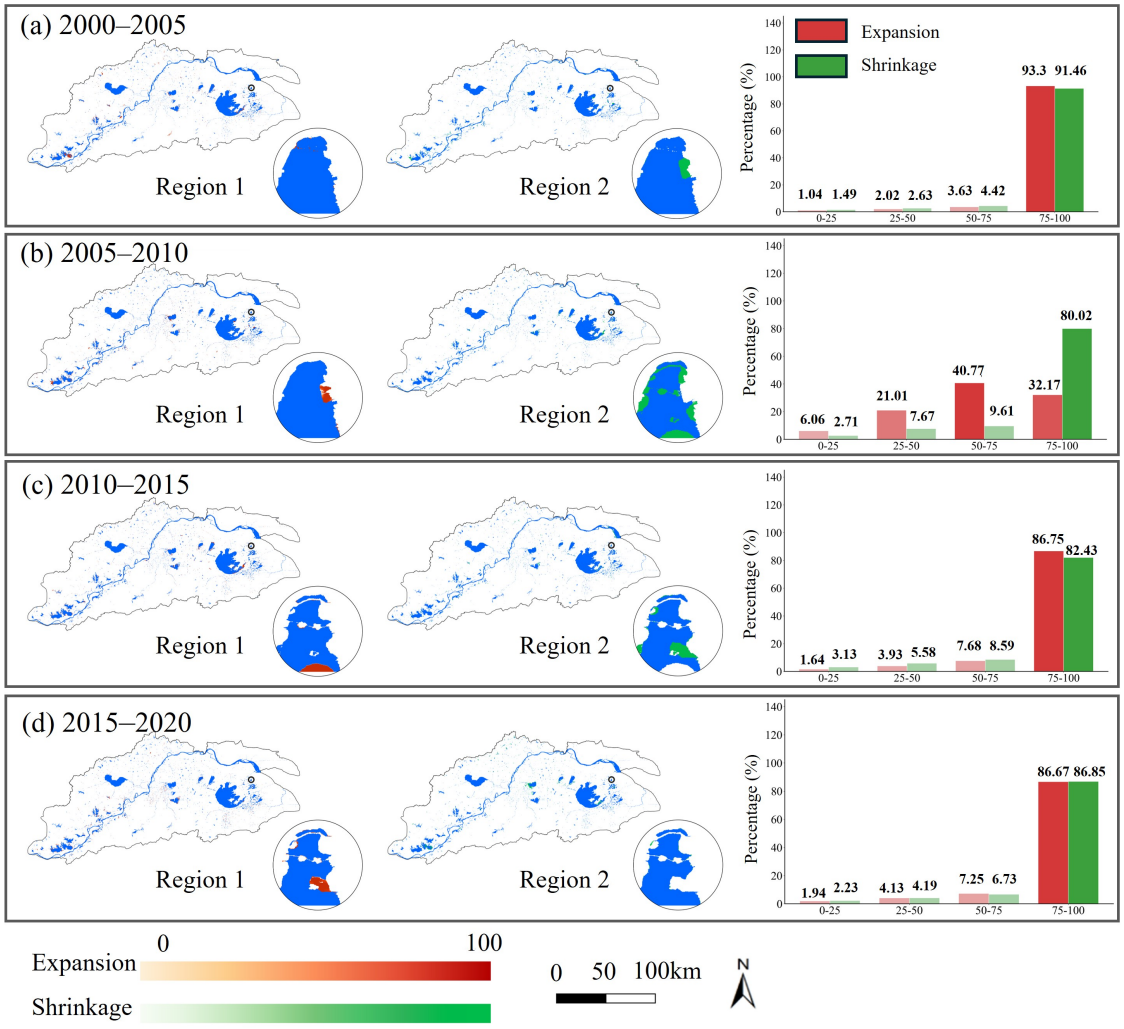


Figure 9. Spatial distribution of SPAT-WVDC for permanent surface water in the LYRB during 2000–2020 (left: SPAT-WVDC index for expansion; middle: SPAT-WVDC index for shrinkage; right: pixel statistics of SPAT-WVDC index for expansion and shrinkage. Blue areas represent common water bodies present in both years): (**a**) 2000–2005. (**b**) 2005–2010. (**c**) 2010–2015. (**d**) 2015–2020.

Local hotspot analysis also showed alternating expansion and shrinkage across successive periods. For instance, the East Taihu (Area 2) expanded significantly during 2010–2015 but shrank during 2015–2020, whereas the Longgan Lake region (Area 1) shifted from shrinkage in 2000 to 2005 to expansion in 2005 to 2010. Generally, the basin-scale and pixel-scale results reveal a clear scale-dependent pattern: basin-scale expansion of permanent surface water often co-occurred with localized fragmentation, while expansion and shrinkage followed different spatial pathways.

4.2.3. Changing Driver Associations Across Periods

The GAM results show a relatively stable but temporally varying explanatory structure across the four study periods (Tables S2–S5). The ADE remained relatively stable, ranging from 45.7% to 50.7%, with adjusted R^2 values ranging from 0.443 to 0.491. NDVI emerged as the predictor with the highest explanatory power across all periods, independently explaining 26.2% to 38.6% of the deviance, with its largest contribution occurring during the 2015–2020 period.

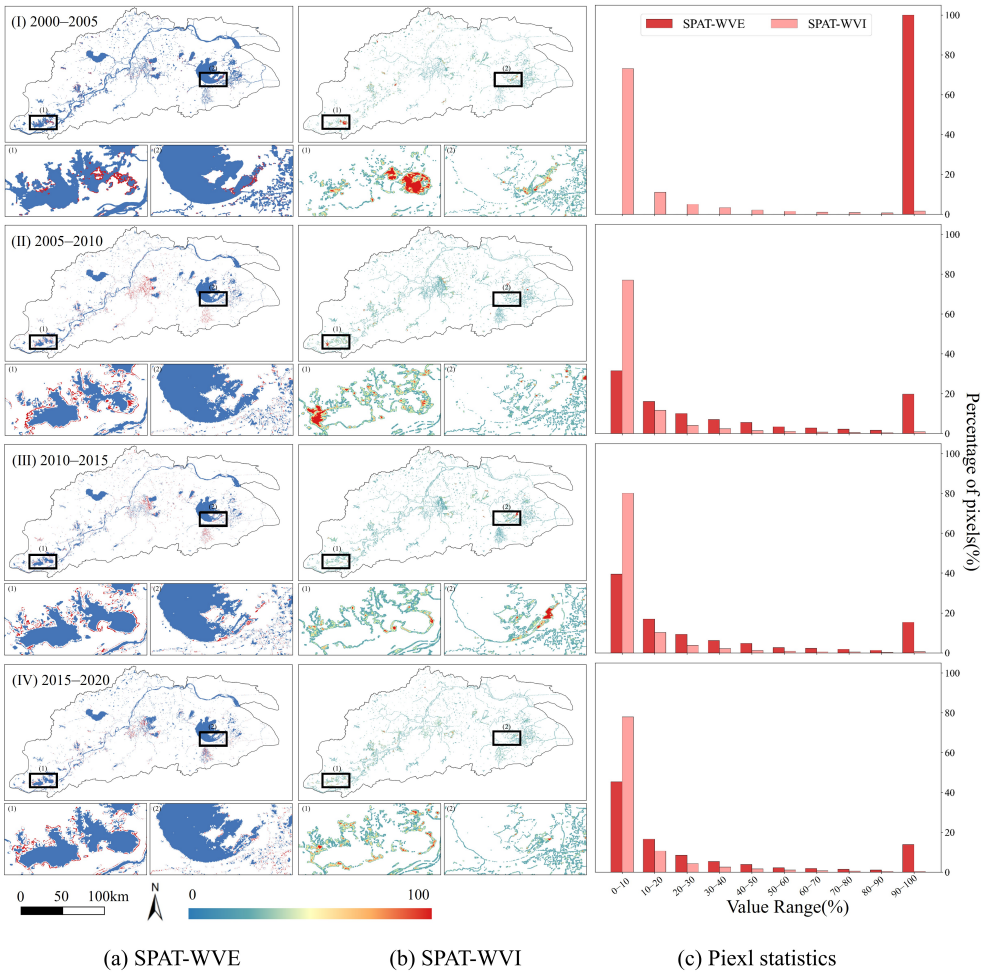


Figure 10. Pixel-level expansion intensity and extent of permanent surface water in the LYRB (2000–2020). (**a**) Results of SPAT-WVE index for expansion. (**b**) Results of SPAT-WVI index for expansion. (**c**) Pixel statistics of SPAT-WVE and SPAT-WVI indices for expansion.

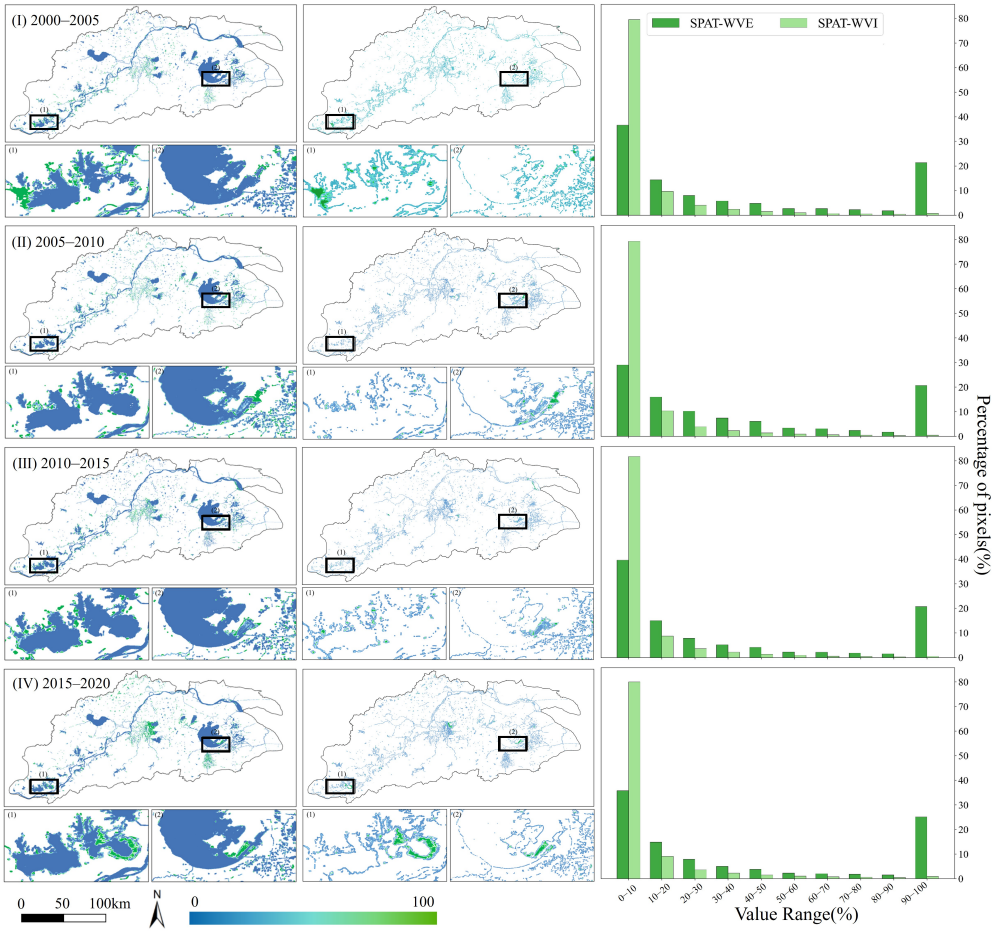
Beyond NDVI, the changing rank and marginal contribution of secondary drivers indicated clear period-specific differences in the explanatory structure of permanent surface-water dynamics (Table 4).

Table 4. Major driving factors of permanent surface-water change from 2000 to 2020.

Period	Primary Driving Factor	Secondary Driving Factors	Cumulative ADE (%)
2000–2005	NDVI	Det, Dpre	49.6
2005–2010	NDVI	Det, POP, Dpre	45.7
2010–2015	NDVI	HAI, Dtem	47.2
2015–2020	NDVI	HAI, Drail, Dpre, POP	48.9

Between 2000 and 2005, evaporation and precipitation were the highest-ranked secondary factors, suggesting a stronger association with hydro-climatic variability than with anthropogenic variables. From 2005 to 2010, the explanatory structure became more mixed, with population density (POP) rising to the fourth-ranked predictor (ADE = 41.2%). During the subsequent 2010–2015 period, human activity intensity (HAI) rose sharply to Rank 2 (Table 4), while temperature also became more prominent. This shift indicates that later-stage variation was increasingly associated with local human activity and land-surface conditions, rather than with hydro-climatic variables alone. In 2015–2020, transportation accessibility (Drail) and population density (POP) replaced hydro-climatic

variables among the highest-ranked secondary factors. Although hydro-climatic variables remained relevant, later-stage models showed stronger contributions from accessibility- and population-related variables. Notably, GDP showed limited improvement in model fit across all periods, suggesting that direct economic output alone was less closely associated with spatial variation in permanent surface water than variables related to human presence, accessibility, and local land-surface modification.



(a) SPAT-WVE (b) SPAT-WVI (c) Piexl statistics

Figure 11. Pixel-level shrinkage intensity and extent of permanent surface water in the LYRB (2000–2020). (**a**) Results of SPAT-WVE index for shrinkage. (**b**) Results of SPAT-WVI index for shrinkage. (**c**) Pixel statistics of SPAT-WVE and SPAT-WVI indices for shrinkage.

5. Discussion

5.1. Multi-Scale Structural Reorganization of Permanent Surface Water

A central result of this study is that basin-scale area trends alone were insufficient to represent the hydrological evolution of permanent surface water in the LYRB. Although the total area of permanent surface water expanded during several periods, both the landscape metrics and the pixel-level indices showed that this expansion was often accompanied by increased shape complexity, reduced aggregation, and localized fragmentation. This means that area increase did not necessarily imply improved structural integrity of the regional water system.

This scale-dependent pattern provides an important hydrological perspective for highly modified river–lake systems. Previous regional studies have shown that surface water or inundation dynamics may vary substantially within the same basin or floodplain–lake system, and that large-scale summaries can overlook strong internal heterogeneity [20].

The present study extends this perspective by focusing specifically on permanent surface water in the lower Yangtze and showing that basin-scale expansion could coexist with pixel-scale fragmentation. Compared with broader Yangtze Basin studies that mainly emphasize redistribution of total surface-water area [19], the present results show that stable water bodies in the lower basin may undergo structural reorganization even when the basin-scale area appears to increase. In this sense, the main contribution of the basin-to-pixel framework is not only to map annual permanent water, but also to reveal localized structural change that would remain hidden if the analysis relied only on basin-wide totals.

The pixel-level results further clarify this structural reorganization. Expansion was most frequently expressed through scattered small patches, whereas shrinkage was concentrated along the margins of existing water bodies, especially in littoral and shallow-water zones. These patterns suggest that water gain and water loss did not occur as simple mirror processes. Instead, they followed different spatial pathways and together produced a pronounced spatial asymmetry in the evolution of permanent surface water. The alternation of expansion and shrinkage hotspots in areas such as East Taihu and Longgan Lake further indicates that local structural change was not monotonic, even when basin-scale trends appeared more orderly. Taken together, these results suggest that basin-scale area statistics alone may overlook important aspects of permanent surface-water change, particularly localized fragmentation and boundary retreat within stable water systems.

5.2. Changing Driver Associations in a Highly Modified Basin

The GAM results indicate that the explanatory structure of permanent surface-water dynamics changed through time. Hydro-climatic variables were relatively more prominent in the early stage, whereas land-surface and anthropogenic variables became more important in the later periods [34]. This pattern should not be interpreted as evidence of an abrupt regime shift, but it does suggest that later-stage permanent surface-water dynamics in the LYRB were less adequately described by hydro-climatic variability alone.

The persistent dominance of NDVI across all four periods is particularly noteworthy. However, NDVI should not be interpreted too narrowly as a direct ecological or hydrological control. In the context of the LYRB, it more likely reflects a broader set of land-surface reconfiguration [35]. The dominance of NDVI therefore suggests that long-term permanent surface-water dynamics in the region were closely linked to changing land-surface conditions throughout the study period.

At the same time, the increasing prominence of variables such as human activity intensity, population density, and transportation accessibility in the later periods indicates that human-modified landscape conditions became more relevant to the observed spatial variation in permanent surface-water. This interpretation is consistent with the physical setting of the lower Yangtze, where river–lake networks, floodplain edges, and nearshore zones have been strongly affected by urban expansion, hydraulic engineering, and land development [3]. Similar regional studies have also shown that surface-water dynamics can be associated with changing environmental controls rather than a single stable set of drivers [21]. In the LYRB, the results suggest a gradual shift in explanatory emphasis from hydro-climatic variables toward a stronger joint influence of land-surface and anthropogenic conditions.

This interpretation is also supported by the spatial results. The co-occurrence of small-patch expansion, marginal retreat of existing water bodies, and alternating hotspot behavior suggests that the changing driver structure was expressed not only in statistical associations, but also in the spatial organization of stable water bodies.

5.3. Hydrological Implications for Basin Dynamics and Modeling

Although this study did not implement a hydrological or hydrodynamic model, the observed permanent surface-water dynamics can still be interpreted as the spatial expression of broader basin processes. Satellite observations of surface-water extent provide spatial evidence for hydrological states and scale-dependent water-area dynamics [20]. Hydrological models usually describe process variables such as runoff, streamflow, water-level fluctuation, floodplain storage, and regulation, whereas remote sensing records their spatial expression through water extent and configuration. Therefore, permanent water area, shoreline retreat, fragmentation, and small-patch expansion are not directly equivalent to discharge or water level, but they provide complementary evidence of how hydrological and human-regulated processes are expressed across the landscape.

In the LYRB, the decline–recovery–stabilization trajectory likely reflects the combined influence of basin-water balance, lake–river connectivity, water-level regulation, and land-surface modification. Previous studies have shown that surface-water area can be linked to hydrological fluxes [21], and that eco-hydrological processes in the Yangtze River Basin are jointly shaped by climate variability and human activities [34]. The coexistence of basin-scale expansion and pixel-scale fragmentation further suggests that permanent surface-water change was not controlled by a single basin-wide driver, but by interactions between regional hydrological variability and localized human modification. Future work could couple the basin-to-pixel framework with hydrological or hydrodynamic model outputs to test whether fragmentation, shoreline retreat, and expansion hotspots correspond to modeled changes in basin water balance, hydraulic connectivity, and regulation intensity.

5.4. Uncertainties and Implications for Regional Hydrological Monitoring

Several uncertainties remain and should be acknowledged. The extraction of permanent surface water from medium-resolution optical imagery is still affected by mixed pixels, turbidity, algal blooms, and urban shadow contamination, especially in narrow channels and boundary zones [15,36]. Although the pooled accuracy comparison and scene-based visual assessment supported the robustness of the proposed method under representative complex conditions, the WIF-threshold sensitivity analysis showed that threshold-related uncertainty could be amplified in shallow, transitional, and boundary-complex environments, particularly in S4. The boundary-buffer analysis further indicated that most changed pixels were located close to water-body boundaries, suggesting that uncertainty mainly affects local boundary delineation and transitional water pixels rather than producing a spatially uniform error across the basin. Therefore, the main basin-scale conclusions are unlikely to be driven by classification uncertainty alone, but local estimates of shoreline retreat, small-patch expansion, and marginal fragmentation should be interpreted with caution.

In addition, the present analysis focuses on annual permanent water and therefore does not capture short-term hydrological regulation or event-scale fluctuations. This temporal aggregation may smooth seasonal water-level changes, local engineering effects, and episodic hydrological events that are relevant at shorter timescales. The GAM results also identify changing explanatory associations rather than causal mechanisms; stronger causal interpretation would require additional process-based analyses or causal-inference approaches [37]. Despite these limitations, the basin-to-pixel framework provides a useful approach for monitoring highly modified river–lake systems. It shows that basin-scale statistics should be interpreted together with structural indicators that reveal fragmentation, boundary retreat, and small-patch dynamics, especially in boundary-rich and transitional water environments where classification uncertainty and real hydrological change may overlap.

6. Conclusions

This study analyzed permanent surface-water dynamics in the LYRB during 2000–2020 using a basin-to-pixel framework that linked annual water mapping, multi-scale spatial analysis, and driver interpretation. The framework combined adaptive threshold-based extraction, multi-scale spatial metrics, pixel-level SPAT indices, and GAM analysis to examine both basin-scale trends and localized structural changes.

The results revealed that permanent surface water in the LYRB followed a clear decline–recovery–stabilization trajectory, with an average area of 8239 km^2 during the study period. Basin-scale expansion often co-occurred with increased pixel-scale fragmentation and decreased spatial connectivity, indicating that area increase did not necessarily imply improved structural integrity of the regional water system. Expansion was mainly expressed through scattered water patches, whereas shrinkage was concentrated along the margins of existing water bodies. Finally, the explanatory structure of permanent surface-water dynamics changed through time. NDVI remained the strongest explanatory variable across all stages, while land-surface and anthropogenic factors became more prominent in the later stages relative to hydro-climatic variables.

Overall, the results show that basin-scale area statistics alone are insufficient to describe the full evolution of permanent surface water in a highly modified river–lake system. By linking long-term area trends with localized structural diagnostics, the basin-to-pixel framework provides a useful multi-scale approach for understanding permanent surface-water change in highly modified river–lake basins.

Supplementary Materials: The following supporting information can be downloaded at: https://www.mdpi.com/article/10.3390/w18151854/s1, Figure S1: Yearly counts of Landsat satellite images obtained for the study area; Table S1: Datasets used in this study; Table S2: Ranking of driving factors influencing permanent surface water change based on GAM (2000–2005); Table S3: Ranking of driving factors influencing permanent surface water change based on GAM (2005-2010); Table S4: Ranking of driving factors influencing permanent surface water change based on GAM (2010–2015); Table S5: Ranking of driving factors influencing permanent surface water change based on GAM (2015–2020); Table S6. WIF-threshold sensitivity analysis across six representative complex scenes; Table S7: Proportions of changed, expansion, and shrinkage pixels located within 30 m and 60 m water-boundary buffers

Author Contributions: J.Y.: Methodology, Investigation, Writing—original draft. Y.T.: Investigation, Writing—original draft, Software. Y.L.: Conceptualization, Writing—review & editing. C.G.: Methodology, Data curation, Validation, Visualization. H.X.: Writing—review & editing, Project administration. All authors have read and agreed to the published version of the manuscript.

Funding: This study was funded by the Fundamental and Interdisciplinary Disciplines Breakthrough Plan of the Ministry of Education of China (Grant No. JYB2025XDXM908).

Data Availability Statement: The original contributions presented in this study are included in the article/Supplementary Material. Further inquiries can be directed to the corresponding author.

Conflicts of Interest: The authors declare no conflict of interest.

References

1. Kulkarni, R.; Khare, K.; Khanum, H. Detecting, extracting, and mapping of inland surface water using Landsat 8 Operational Land Imager: A case study of Pune district, India. *F1000Research* **2022**, *11*, 774. [CrossRef] [PubMed]
2. Niu, Z.; Liu, Y.; Feng, L.; Qin, P.; Jiang, W.; Feng, Y.; Hu, Y.; Xue, H. Spatio-temporal distribution characteristics of different types of compound extreme climate events in the Yangtze River Basin. *Nat. Hazards* **2025**, *121*, 9261–9280. [CrossRef]
3. Deng, X.; Xu, Y.; Han, L.; Song, S.; Yang, L.; Li, G.; Wang, Y. Impacts of urbanization on river systems in the Taihu Region, China. *Water* **2015**, *7*, 1340–1358. [CrossRef]

4. Wang, S.; Baig, M.H.A.; Zhang, L.; Jiang, H.; Ji, Y.; Zhao, H.; Tian, J. A simple enhanced water index (EWI) for percent surface water estimation using Landsat data. *IEEE J. Sel. Top. Appl. Earth Obs. Remote Sens.* **2015**, *8*, 90–97. [CrossRef]
5. Wu, P.; Fu, J.; Yi, X.; Wang, G.; Mo, L.; Maponde, B.T.; Liang, H.; Tao, C.; Ge, W.; Jiang, T.; et al. Research on water extraction from high resolution remote sensing images based on deep learning. *Front. Remote Sens.* **2023**, *4*, 1283615. [CrossRef]
6. Zhao, F.; Feng, S.; Xie, F.; Zhu, S.; Zhang, S. Extraction of long time series wetland information based on Google Earth Engine and random forest algorithm for a plateau lake basin–A case study of Dianchi Lake, Yunnan Province, China. *Ecol. Indic.* **2023**, *146*, 109813. [CrossRef]
7. Rajeswari, S.; Rathika, P. Emerging methodologies in waterbody delineation: An In-depth review. *Int. J. Remote Sens.* **2024**, *45*, 5789–5819. [CrossRef]
8. McFeeters, S.K. The use of the Normalized Difference Water Index (NDWI) in the delineation of open water features. *Int. J. Remote Sens.* **1996**, *17*, 1425–1432. [CrossRef]
9. Xu, H. Modification of normalised difference water index (NDWI) to enhance open water features in remotely sensed imagery. *Int. J. Remote Sens.* **2006**, *27*, 3025–3033. [CrossRef]
10. Feyisa, G.L.; Meilby, H.; Fensholt, R.; Proud, S.R. Automated Water Extraction Index: A new technique for surface water mapping using Landsat imagery. *Remote Sens. Environ.* **2014**, *140*, 23–35. [CrossRef]
11. Jia, Y.Y.; Duan, H.F.; Yan, X.F. Effect of Hydro-geomorphological Environments on Surface Water Areas Extraction. *Water Resour. Manag.* **2025**, *39*, 5461–5479. [CrossRef]
12. Zhang, W.; Guo, J.; Liu, Z.; Shi, L.; Gong, Z.; Zhang, D. Analysis of Spatial and Temporal Shoreline Changes and Reclamation in the Qinzhou Bay and the Manila Bay. *Trop. Geogr.* **2025**, *45*, 489–503.
13. Pekel, J.F.; Cottam, A.; Gorelick, N.; Belward, A.S. High-resolution mapping of global surface water and its long-term changes. *Nature* **2016**, *540*, 418–422. [CrossRef] [PubMed]
14. Zhang, W.; Zhang, Z.; Wei, X.; Hu, Y.; Li, Y.; Meng, L. Long-term spatiotemporal changes of surface water and its influencing factors in the mainstream of Han River, China. *J. Hydrol. Reg. Stud.* **2022**, *40*, 101009. [CrossRef]
15. Mao, W.; Yang, K.; Zhang, W.; Wang, Y.; Li, M. High-resolution global water body datasets underestimate the extent of small rivers. *Int. J. Remote Sens.* **2022**, *43*, 4315–4330. [CrossRef]
16. Zhao, B.; Wang, L. Surface water monitoring from 1984 to 2021 based on Landsat time-series images and Google Earth Engine. *Heliyon* **2024**, *10*, e36660. [CrossRef] [PubMed]
17. Xiao, Z.; Li, R.; Ding, M.; Cai, P.; Guo, J.; Fu, H.; Zhang, X.; Song, X. Unveiling the hidden dynamics of intermittent surface water: A remote sensing framework. *Remote Sens. Environ.* **2024**, *311*, 114285. [CrossRef]
18. Jin, H.; Fang, S.; Chen, C. Mapping of the Spatial scope and water quality of surface water based on the Google Earth engine cloud platform and Landsat time series. *Remote Sens.* **2023**, *15*, 4986. [CrossRef]
19. Chang, L.; Cheng, L.; Li, S.; Guo, Z.; Liu, Y.; Zhang, L. Reservoir dominated spatio-temporal changes of the surface water area in the Yangtze River Basin during past three decades. *J. Hydrol. Reg. Stud.* **2024**, *55*, 101948. [CrossRef]
20. Wang, J.; Zhang, Y.; Yu, H.; Zheng, B.; Wan, W. Multi-scale characteristics and driving mechanisms of spatio-temporal variations in the water area of the largest floodplain lake in China. *J. Hydrol. Reg. Stud.* **2026**, *64*, 103298. [CrossRef]
21. Ahmmed, M.H.; Mahmood, T.H.; Archambault, A.L.; Wainty, S. Relationships between surface water area and hydrologic fluxes in a cold region terminal lake basin. *J. Hydrol. Reg. Stud.* **2025**, *62*, 102766. [CrossRef]
22. Li, P.; Yu, Z.; Jiang, P.; Wu, C. Spatiotemporal characteristics of regional extreme precipitation in Yangtze River basin. *J. Hydrol.* **2021**, *603*, 126910. [CrossRef]
23. Jia, H.; Chen, F.; Pan, D.; Du, E.; Wang, L.; Wang, N.; Yang, A. Flood risk management in the Yangtze River basin—Comparison of 1998 and 2020 events. *Int. J. Disaster Risk Reduct.* **2022**, *68*, 102724. [CrossRef]
24. Guo, S.; Du, P.; Meng, Y.; Wang, X.; Tang, P.; Lin, C.; Xia, J. Dynamic monitoring on flooding situation in the Middle and Lower Reaches of the Yangtze River Region using Sentinel-1A time series. *Natl. Remote Sens. Bull.* **2021**, *25*, 2127–2141. [CrossRef]
25. Otsu, N. A threshold selection method from gray-level histograms. *IEEE Trans. Syst. Man, Cybern.* **1979**, *9*, 62–66. [CrossRef]
26. Zhou, Y.; Dong, J.; Xiao, X.; Liu, R.; Zou, Z.; Zhao, G.; Ge, Q. Continuous monitoring of lake dynamics on the Mongolian Plateau using all available Landsat imagery and Google Earth Engine. *Sci. Total Environ.* **2019**, *689*, 366–380. [CrossRef] [PubMed]
27. Hao, Z.; Foody, G.; Ge, Y.; Cai, X.; Du, Y.; Ling, F. DeepWaterFraction: A globally applicable, self-training deep learning approach for percent surface water area estimation from Landsat mission imagery. *J. Hydrol.* **2024**, *638*, 131512. [CrossRef]
28. Chen, A.; Yao, L.; Sun, R.; Chen, L. How many metrics are required to identify the effects of the landscape pattern on land surface temperature? *Ecol. Indic.* **2014**, *45*, 424–433. [CrossRef]
29. Jia, Y.; Tang, L.; Xu, M.; Yang, X. Landscape pattern indices for evaluating urban spatial morphology—A case study of Chinese cities. *Ecol. Indic.* **2019**, *99*, 27–37. [CrossRef]
30. Hu, J.; Zhang, J.; Li, Y. Exploring the spatial and temporal driving mechanisms of landscape patterns on habitat quality in a city undergoing rapid urbanization based on GTWR and MGWR: The case of Nanjing, China. *Ecol. Indic.* **2022**, *143*, 109333. [CrossRef]

31. Fan, Q.; Lu, Q.; Liu, B.; Li, J.; Ping, X.; Yang, X. Research on the centre of gravity after "Transfer-Conversion-Changes" in different land use types during 2010–2020. *Sci. Rep.* **2025**, *15*, 21722. [CrossRef] [PubMed]
32. McGarigal, K.; Cushman, S.A.; Neel, M.C.; Ene, E. *FRAGSTATS: Spatial Pattern Analysis Program for Categorical Maps*; University of Massachusetts: Amherst, MA, USA, 2002.
33. Vaca, R.A.; Golicher, D.J.; Rodiles-Hernández, R.; Castillo-Santiago, M.Á.; Bejarano, M.; Navarrete-Gutiérrez, D.A. Drivers of deforestation in the basin of the Usumacinta River: Inference on process from pattern analysis using generalised additive models. *PLoS ONE* **2019**, *14*, e0222908. [CrossRef] [PubMed]
34. He, N.; Guo, W.; Lan, J.; Yu, Z.; Wang, H. The impact of human activities and climate change on the eco-hydrological processes in the Yangtze River basin. *J. Hydrol. Reg. Stud.* **2024**, *53*, 101753. [CrossRef]
35. Qu, S.; Wang, L.; Lin, A.; Zhu, H.; Yuan, M. What drives the vegetation restoration in Yangtze River basin, China: Climate change or anthropogenic factors? *Ecol. Indic.* **2018**, *90*, 438–450. [CrossRef]
36. Zhao, C.; Wei, H.; Feyisa, G.L.; de Castro Tayer, T.; Ma, G.; Wu, H.; Pan, Y. Evaluating spectral indices for water extraction: Limitations and contextual usage recommendations. *Int. J. Appl. Earth Obs. Geoinf.* **2025**, *139*, 104510. [CrossRef]
37. Liang, H.; Wang, W.; Liu, D.; Chen, B.; Guo, L.; Liu, H.; Yu, S.; Zhang, D. Inferring causal associations in hydrological systems: A comparison of methods. *Stoch. Environ. Res. Risk Assess.* **2025**, *39*, 2427–2448. [CrossRef]

Disclaimer/Publisher's Note: The statements, opinions and data contained in all publications are solely those of the individual author(s) and contributor(s) and not of MDPI and/or the editor(s). MDPI and/or the editor(s) disclaim responsibility for any injury to people or property resulting from any ideas, methods, instructions or products referred to in the content.